Acquisition and Automated 3-D Segmentation of Respiratory/Cardiac-Gated PET Transmission Images

BW Reutter, GJ Klein, KM Brennan, and RH Huesman

Center for Functional Imaging, Lawrence Berkeley National Laboratory
University of California, One Cyclotron Road, Berkeley, CA 94720

Abstract

To evaluate the impact of respiratory motion on attenuation correction of cardiac PET data, we acquired and automatically segmented gated transmission data for a dog breathing on its own under gas anesthesia.

Data were acquired for 20 min on a CTI/Siemens ECAT EXACT HR (47-slice) scanner configured for 12 gates in a static study. Two respiratory gates were obtained using data from a pneumatic bellows placed around the dog's chest, in conjunction with 6 cardiac gates from standard EKG gating. Both signals were directed to a LabVIEW-controlled Macintosh, which translated them into one of 12 gate addresses. The respiratory gating threshold was placed near end-expiration to acquire 6 cardiac-gated datasets at end-expiration and 6 cardiac-gated datasets during breaths. Breaths occurred about once every 10 sec and lasted about 1-1.5 sec.

For each respiratory gate, data were summed over cardiac gates and torso and lung surfaces were segmented automatically using a differential 3-D edge detection algorithm. Three-dimensional visualizations showed that lung surfaces adjacent to the heart translated 9 mm inferiorly during breaths.

Our results suggest that respiration-compensated attenuation correction is feasible with a modest amount of gated transmission data and is necessary for accurate quantitation of high-resolution gated cardiac PET data.

I. INTRODUCTION

Over the past 20 years, the spatial resolution attainable by positron emission tomography (PET) systems has improved dramatically. With this improved resolution, there is the potential to obtain detailed maps of myocardial perfusion and metabolism. However, this potential remains largely unfulfilled since current data acquisition and analysis strategies do not account for the respiratory and contractile motion of the heart, which has an amplitude more than twice the 4-5 mm resolution of contemporary commercial scanners. While the resulting blurred images are reasonable qualitative estimates of the left ventricular myocardial activity, they fall far short of the high-resolution quantitative images that are potentially attainable with modern PET systems.

The effects of respiratory motion of the heart have been virtually ignored in cardiac emission tomography, although the problem has been recognized and was described in 1982 [1]. Respiratory motion of the diaphragm and heart has been estimated to be approximately 15 mm in a human in the supine position during tidal breathing [2, 3]. The effects of gross patient motion have been studied, particularly with respect to the misalignment that often results between transmission and emission data in PET [4, 5, 6]. A 20 mm patient motion between transmission and emission scans produced changes of up to 30% in regional myocardial activity estimates [5].

In order to compensate for the motion of the heart, we have developed methods for separating events during both transmission and emission data acquisition according to respiratory and electrocardiogram (EKG) cues. Thus, emission data can be analyzed using properly registered attenuation correction factors (ACFs).

When data acquired during a typical 20 min transmission study are separated into multiple respiratory states, however, the resulting ACFs for each state are noisy due to relatively low counting statistics. To obtain less noisy ACFs, techniques have been developed to segment noisy transmission images into air, soft tissue, and lung based on semi-automatic differential-based 2-D edge detection [7], automatic threshold-based pixel classification [8, 9, 10], and neural network pattern classification [11] . This patient segmentation typically is smoothed with a Gaussian to obtain a map with resolution comparable to the emission data, and is then combined with a map for the tomograph bed obtained from a separate high-statistics transmission study performed without the patient in the scanner. The combined map is then forward-projected to obtain less noisy ACFs.

To supplement these techniques, we have developed efficient multi-scale differential 3-D image processing techniques which automatically create time-varying geometric models of the torso and lung surfaces from respiratory-gated transmission data. A pixel can first be classified according to which surface (if any) most immediately encloses the pixel during a given respiratory state and then be assigned an appropriate attenuation coefficient.

II. HARDWARE GATING

In collaboration with CTI Inc., we modified the software and hardware of our CTI/Siemens ECAT EXACT HR (47-slice) tomograph to support prospective cardiac and respiratory gating. The modified tomograph front panel accepts four TTL inputs which encode a desired acquisition gate. As these inputs change, tomograph events are directed to one of up to 12 different transmission data buffers in memory, where each buffer represents the data from the 47 2-D slices acquired

for that gate. Up to 16 different buffers can be used for gated emission data acquisition.

To supply the appropriate 4-bit gating address to the scanner, we implemented a hardware and software front end. The front end characterizes the cardiac and respiratory state of the subject being imaged from external analog cues using the LabVIEW real-time environment on a Macintosh workstation, as well as custom analog signal processing hardware. The cardiac signal is derived from standard EKG monitors. This analog EKG signal is directed to signal processing hardware which generates a pulse at each R-wave. Respiratory monitoring is achieved using a pneumatic bellows originally designed for magnetic resonance image (MRI) scanners (General Electric part number E8811ED: Bellows Assembly for Respiratory Compensation Packages). The bellows is secured around the patient's chest, and the analog signal from a pressure transducer connected to the bellows is amplified and input along with the R-wave pulse to a National Instruments NB-MIO-16 data acquisition board resident in the Macintosh. The Macintosh samples the signals, typically at 10 Hz for the respiratory input, and at over 600 Hz for the cardiac input. For each sample, a respiratory state is set based upon the absolute amplitude of the pressure transducer signal, and the cardiac state is set based upon the time since the last R-wave. The cardiac and respiratory states are used to select an output gating state from a 2-D lookup table. This state is encoded by the National Instruments board as four binary outputs and directed to the ECAT scanner.

Using this gating configuration with two respiratory gates and six cardiac gates, a 20 min transmission scan was acquired for a dog breathing on its own under gas anesthesia. Only two respiratory gates were chosen because the anesthetized dog remained in the expiration state about 85-90% of the time, taking only occasional, relatively shallow, quick breaths. The heart rate of the dog was approximately 115 beats per min, and cardiac gates were set to 60 msec intervals starting at the R-wave.

III. AUTOMATED 3-D TRANSMISSION IMAGE SEGMENTATION

Our gated transmission image analysis is based upon a body of work which has sought to improve image segmentation by combining estimates of the differential properties of an image with knowledge about the expected contrast between structures and the expected locations, shapes, and sizes of the structures of interest.

Candidate boundaries for structures of interest have been constructed by linking together points in a dataset where the image intensity is changing rapidly. Points of locally maximum (or near-maximum, based on other constraints) estimated image gradient vector magnitude have been linked [12, 13, 14, 15, 16, 17], as have zero-crossing points obtained in response to a second-order differential operator such as the Laplacian or the second derivative in the direction of the gradient [18, 19, 20, 21, 22, 23]. The medial axes and widths of structures have been extracted by pairing boundary

points on opposite sides of the structures, using first- and second-order differential operators [24]. Other geometric primitives, such as n-junctions, have been extracted using higher-order differential operators [25]. Typically, these operators are composed of Gaussian derivative kernels, which smooth the data prior to performing differentiation. The Gaussian scale parameter (standard deviation) σ is varied systematically to optimize the response of the operator with respect to the size and detail of the structures of interest [26, 27, 21].

As the size of medical image datasets continues to grow, computational efficiency becomes more of an issue, particularly with multi-scale processing techniques. Starting with a 3-D dataset, processing each spatial axis of the data independently at just two scales increases the total amount of data processed by a factor of $2^3 = 8$. As a more computationally efficient alternative to Gaussian derivative filtering, we and others have been investigating the use of wavelet kernels based on the uniform B-spline basis function. The uniform B-spline has scaling properties that allow an implementation of filter kernels with geometrically increasing standard deviation σ, using fixed computation at each scale [28, 29]. By comparison, iteratively filtering with the same Gaussian results in only a sub-linear increase in σ for a fixed amount of computation. The kth-order uniform B-spline basis function, $\Pi^{*k}(x)$, is the piecewise $(k-1)$st-degree polynomial that is obtained by convolving the rectangle function

$$\Pi(x) = \begin{cases} 1, & -\frac{1}{2} \le x \le \frac{1}{2} \\ 0, & \text{else} \end{cases} \quad (1)$$

with itself $k - 1$ times. The Gaussian is obtained in the limit as the order k approaches infinity.

Using wavelet filter kernels derived from the uniform cubic B-spline basis function, $\Pi^{*4}(x)$, we implemented a 3-D edge detection operator that estimates the second derivative in the gradient direction, weighted by the squared magnitude of the gradient:

$$\|\nabla f\|^2 \left[\frac{\nabla f}{\|\nabla f\|} \cdot \nabla \left[\frac{\nabla f}{\|\nabla f\|} \cdot \nabla f \right] \right] = \sum_{p=1}^{3} \sum_{q=1}^{3} \frac{\partial f}{\partial(x^p)} \frac{\partial f}{\partial(x^q)} \frac{\partial^2 f}{\partial(x^p)\partial(x^q)}, \quad (2)$$

where x^1, x^2, and x^3 denote the spatial coordinates. For convenience, we will also denote these coordinates by x, y, and z, respectively. In 2-D, the second directional derivative operator has been shown to perform better than the Laplacian, $\nabla^2 f$, under a variety of conditions [19, 30].

The first- and second-order partial derivatives of each respiratory-gated transmission dataset were calculated efficiently at multiple spatial scales by convolving with the wavelet filter kernels. Then, candidate anatomical surfaces were constructed by linking together zero-crossing points in the second directional derivative operator output (Equation 2), using an approach similar to Wallin [31]. In our implementation, zero-crossing points for each respiratory
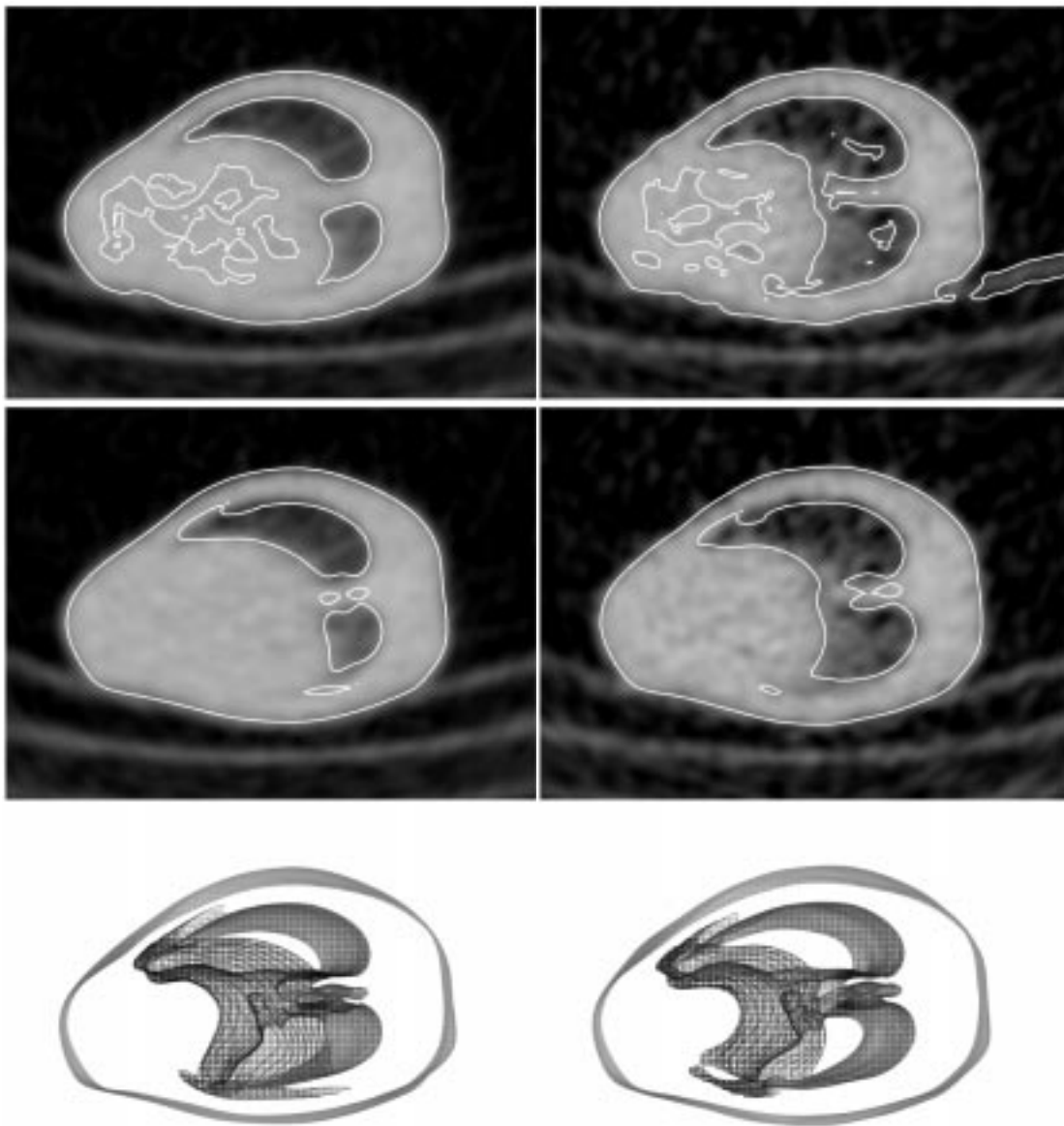
Fig. 1 Upper, Middle: Transverse respiratory-gated canine transmission images superimposed with cross-sections of torso and lung surface models constructed automatically using the 3-D second directional derivative operator (upper left: end-expiration, $11\times11\times7$ operator; upper right: during breaths, $11\times11\times7$ operator; middle left: end-expiration, $23\times23\times15$ operator; middle right: during breaths, $23\times23\times15$ operator). Lower: Inferior views of canine torso and lung surface models constructed automatically using the $23\times23\times15$ operator (lower left: end-expiration; lower right: during breaths). The dog is lying on its right side.

state were first linked together to form spatial contours in the xy (transverse), xz (coronal), and yz (sagittal) image planes. Surfaces were then constructed by linking together the contours. Information about the centroid, bounding box, and average image intensity gradient across each of the contours, as well as each of the surfaces, was stored to facilitate higher-level image analysis.

Each respiratory-gated transmission dataset was composed of 47 contiguous 3.125 mm-thick transverse images. Each transverse image was 128×128 pixels, with pixel size 2.5×2.5 mm. Due to the infrequent shallow breathing of the dog, the length of the data acquisition during breaths totaled

only about 2-3 min, while the length of the data acquisition during end-expiration totaled about 17-18 min. A 3×3 pixel gray-scale morphological opening operator was applied to each transverse image to reduce noise, while preserving intensity transitions associated with tissue boundaries [32].

We then processed each $128\times128\times47$ dataset using the 3-D second directional derivative operator (Equation 2). Surfaces were constructed automatically after discarding the results from the first and last four transverse sections, which were excessively noisy due to boundary effects at the ends of the tomograph. We experimented with a number of different wavelet filter kernel sizes. Figures 1 and 2 show the results of
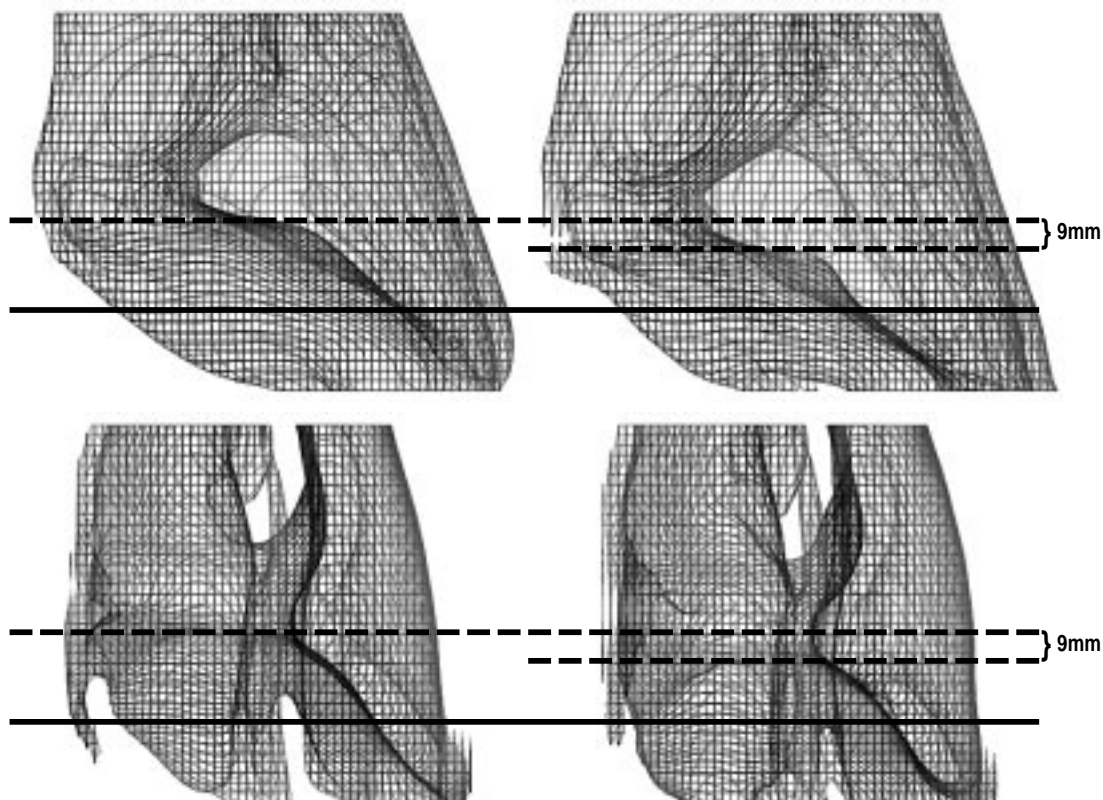
Fig. 2 Upper: Left-lateral views of canine lung surface models constructed automatically using the 23×23×15 second directional derivative operator (upper left: end-expiration; upper right: during breaths). Lower: Anterior views of canine lung surface models constructed automatically using the 23×23×15 operator (lower left: end-expiration; lower right: during breaths). The dashed lines show that the diaphragm translated 9 mm inferiorly during breaths. The solid lines show the position of the transverse images shown in Figure 1.

processing using kernels with supports 11×11×7 pixels (along the x, y, and z axes, respectively) and 23×23×15 pixels. Figure 2 shows that the diaphragm translated 9 mm inferiorly during breaths.

Processing with the 11×11×7 kernels resulted in reasonably accurate torso and lung surface models, as well as some smaller-scale structures due to image noise. Processing with the 23×23×15 kernel resulted in less accurate torso and lung surface models, while eliminating most of the smaller-scale noise structures. With either kernel size, the relatively large, high-contrast, cross-sectional contours associated with the torso and lung surfaces could be identified easily by using the information stored about the centroid, bounding box, and average image intensity gradient across each of the contours. For a given wavelet filter kernel size, the 3-D differential image processing and automated surface construction took about 1.7 min for each respiratory state, on a Silicon Graphics 100 MHz R4000-based Unix workstation.

IV. Segmented Attenuation Correction

Having time-varying geometric models for the torso and lung surfaces, one can assign an attenuation coefficient to a volume element (voxel) according to which surface (if any) most immediately encloses the voxel during a given respiratory state. For voxels outside the chest one can assign a constant coefficient of zero, and for voxels inside the chest and outside the lungs one can assign a constant coefficient appropriate for tissue. Because attenuation within the lungs varies significantly between patients, as well as spatially and with respiratory state, attenuation coefficients inside the lungs can be assigned based on local 3-D averages of voxels completely inside the lungs. A voxel straddling a surface can be assigned an appropriate coefficient based on the relative volumes of materials contained within the voxel. In addition, an attenuation map is needed for the bed. This map can be obtained from a separate high-statistics transmission study performed without the patient in the scanner.

V. Conclusions

A strength of our automated multi-scale differential image processing techniques is that data are analyzed efficiently in 3-D over appropriate spatial scales in an effort to extract and to physically model the time-varying surfaces which bound the torso and lungs. Our structured analysis imposes spatial continuity constraints that complement the information that is available from unstructured image pixel gray-level value alone. Using these methods we obtained good segmentations of images reconstructed from gated transmission data obtained with as little as 3 minutes of acquisition time per gate.

We have embarked on full 4-D structured analysis of gated

human transmission data. Because an awake human breathes more regularly than does an anesthetized dog, sufficient data can be acquired during the intermediate respiratory states to facilitate tracking the more continuously varying motion of the diaphragm and heart. By processing in 4-D the data that we can acquire using 4-5 respiratory gates, we expect that the additional temporal continuity constraint will aid the extraction and tracking of the torso and lung surfaces across space and time.

VI. ACKNOWLEDGMENTS

VII. REFERENCES

[1] M M Ter-Pogossian, S R Bergmann, and B E Sobel. Influence of cardiac and respiratory motion on tomographic reconstructions of the heart: Implications for quantitative nuclear cardiology. *J Comput Assist Tomogr*, 6(6):1148–1155, 1982.

[2] J O Fredrickson, H Wegmüller, R J Herfkens, and N J Pelc. Simultaneous temporal resolution of cardiac and respiratory motion in MR imaging. *Radiology*, 195:169–175, 1995.

[3] Y Wang, S J Riederer, and R L Ehman. Respiratory motion of the heart: Kinematics and the implications for the spatial resolution in coronary imaging. *Magn Reson Med*, 33(5):713–719, 1995.

[4] S-C Huang, E J Hoffman, M E Phelps, and D E Kuhl. Quantitation in positron emission computed tomography: 2. Effects of inaccurate attenuation correction. *J Comput Assist Tomogr*, 3(6):804–814, 1979.

[5] M E McCord, S L Bacharach, R O Bonow, V Dilsizian, A Cuocolo, and N Freedman. Misalignment between PET transmission and emission scans: Its effect on myocardial imaging. *J Nucl Med*, 33(6):1209–1214, 1992.

[6] J L R Andersson, B E Vagnhammar, and H Schneider. Accurate attenuation correction despite movement during PET imaging. *J Nucl Med*, 36(4):670–678, 1995.

[7] S-C Huang, R E Carson, M E Phelps, E J Hoffman, H R Schelbert, and D E Kuhl. A boundary method for attenuation correction in positron computed tomography. *J Nucl Med*, 22(7):627–637, 1981.

[8] E Z Xu, N A Mullani, K L Gould, and W L Anderson. A segmented attenuation correction for PET. *J Nucl Med*, 32(1):161–165, 1991.

[9] S R Meikle, M Dahlbom, and S R Cherry. Attenuation correction using count-limited transmission data in positron emission tomography. *J Nucl Med*, 34(1):143–150, 1993.

[10] M Xu, W K Luk, P D Cutler, and W M Digby. Local threshold for segmenting attenuation correction of PET imaging of the thorax. *IEEE Trans Nucl Sci*, 41(4):1532–1537, 1994.

[11] S K Yu and C Nahmias. Segmented attenuation correction using artificial neural networks in positron tomography. *Phys Med Biol*, 41:2189–2206, 1996.

[12] J Canny. A computational approach to edge detection. *IEEE Trans Patt Anal Machine Intell*, PAMI-8(6):679–698, 1986.

[13] M Kass, A Witkin, and D Terzopoulos. Snakes: Active contour models. *Int J Computer Vision*, 1(4):321–331, 1987.

[14] T L Faber, E M Stokely, R M Peshock, and J R Corbett. A model-based four-dimensional left ventricular surface detector. *IEEE Trans Med Imag*, 10(3):321–329, 1991.

[15] L D Cohen and I Cohen. Finite-element methods for active contour models and balloons for 2-D and 3-D images. *IEEE Trans Patt Anal Machine Intell*, 15(11):1131–1147, 1993.

[16] T L Faber, C D Cooke, J W Peifer, R I Pettigrew, J P Vansant, J R Leyendecker, and E V Garcia. Three-dimensional displays of left ventricular epicardial surface from standard cardiac SPECT perfusion quantitation techniques. *J Nucl Med*, 36(4):697–703, 1995.

[17] D R Thedens, D J Skorton, and S R Fleagle. Methods of graph searching for border detection in image sequences with applications to cardiac magnetic resonance imaging. *IEEE Trans Med Imag*, 14(1):42–55, 1995.

[18] D Marr and E Hildreth. Theory of edge detection. *Proc R Soc Lond B*, 207:187–217, 1980.

[19] R M Haralick. Digital step edges from zero crossing of second directional derivatives. *IEEE Trans Patt Anal Machine Intell*, PAMI-6(1):58–68, 1984.

[20] V R Algazi, B W Reutter, W L G van Warmerdam, and C C Liu. Three-dimensional image analysis and display by space-scale matching of cross sections. *J Opt Soc Am A*, 6(6):890–899, 1989.

[21] W L G van Warmerdam and V R Algazi. Describing 1-D intensity transitions with Gaussian derivatives at the resolutions matching the transition widths. *IEEE Trans Patt Anal Machine Intell*, 11(9):973–977, 1989.

[22] S G Mallat. Multifrequency channel decompositions of images and wavelet models. *IEEE Trans Acoust Speech Signal Processing*, 37(12):2091–2110, 1989.

[23] A Goshtasby and D A Turner. Segmentation of cardiac cine MR images for extraction of right and left ventricular chambers. *IEEE Trans Med Imag*, 14(1):56–64, 1995.

[24] B S Morse, S M Pizer, and A Liu. Multiscale medial analysis of medical images. *Image & Vision Comput*, 12(6):327–338, 1994.

[25] B M ter Haar Romeny, L M J Florack, A H Salden, and M A Viergever. Higher order differential structure of images. *Image & Vision Comput*, 12(6):317–325, 1994.

[26] A P Witkin. Scale-space filtering. *Proc Eighth Int Joint Conf Artif Intell*, pages 1019–1022, 1983.

[27] J Babaud, A P Witkin, M Baudin, and R O Duda. Uniqueness of the Gaussian kernel for scale-space filtering. *IEEE Trans Patt Anal Machine Intell*, PAMI-8(1):26–33, 1986.

[28] S Mallat and S Zhong. Characterization of signals from multiscale edges. *IEEE Trans Patt Anal Machine Intell*, 14(7):710–732, 1992.

[29] M Unser, A Aldroubi, and M Eden. The L_2 polynomial spline pyramid. *IEEE Trans Patt Anal Machine Intell*, 15(4):364–379, 1993.

[30] J De Vriendt. Accuracy of the zero crossings of the second directional derivative as an edge detector. *Multidim Sys Signal Processing*, 4:227–251, 1993.

[31] A Wallin. Constructing surfaces from CT data. *IEEE Computer Graphics & Applications*, 11(6):28–33, 1991.

[32] S R Sternberg. Grayscale morphology. *Computer Vision Graphics Image Processing*, 35(3):333–355, 1986.